Volumetric trans-scale imaging of massive quantity of heterogeneous cell populations in centimeter-wide tissue and embryo

Authors

Taro Ichimura,[1]* Taishi Kakizuka,[1,2] Yoshitsugu Taniguchi,[3] Satoshi Ejima,[3] Yuki Sato,[4] Keiko Itano,[2] Kaoru Seiriki,[5] Hitoshi Hashimoto,[1,5] Ko Sugawara,[6] Hiroya Itoga,[6] Shuichi Onami,[1,6] and Takeharu Nagai[1,2,7]*

Affiliations

[1]Transdimensional Life Imaging Division, Institute for Open and Transdisciplinary Research Initiatives, Osaka University, Yamadaoka 2-1, Suita, Osaka 565-0871, Japan.

[2]Department of Biomolecular Science and Engineering, SANKEN, Osaka University, Mihogaoka 8-1, Ibaraki, Osaka 567-0047, Japan.

[3]SIGMAKOKI CO., LTD., 1-19-9 Midori, Sumida-ku, Tokyo 130-0021, Japan.

[4]Department of Anatomy and Cell Biology, Graduate School of Medical Sciences, Kyushu University, Maidashi 3-1-1, Higashi-ku, Fukuoka 812-8582, Japan.

[5]Laboratory of Molecular Neuropharmacology, Graduate School of Pharmaceutical Sciences, Osaka University, Yamadaoka 1-6, Suita, Osaka 565-0871, Japan.

[6]Laboratory for Developmental Dynamics, RIKEN Center for Biosystems Dynamics Research, Minatojima-minamimachi 2-2-3, Chuo-ku, Kobe, Hyogo 650-0047, Japan.

[7]Research Institute for Electronic Science, Hokkaido University, Kita 20, Nishi 10, Kita-ku, Sapporo, Hokkaido 001-0020, Japan.

*Email address: ichimura@otri.osaka-u.ac.jp, ng1@sanken.osaka-u.ac.jp

Abstract

We established a volumetric trans-scale imaging system with an ultra-large field-of-view (FOV) that enables simultaneous observation of millions of cellular dynamics in centimeter-wide three-dimensional (3D) tissues and embryos. Using a custom-made giant lens system with a magnification of 2× and a numerical aperture (NA) of 0.25, and a CMOS camera with

more than 100 megapixels, we built a trans-scale scope AMATERAS-2, and realized fluorescence imaging with a transverse spatial resolution of approximately 1.1 μm across an FOV of approximately 1.5 × 1.0 cm^2. The 3D resolving capability was realized through a combination of optical and computational sectioning techniques tailored for our low-power imaging system. We applied the imaging technique to 1.2 cm-wide section of mouse brain, and successfully observed various regions of the brain with sub-cellular resolution in a single FOV. We also performed time-lapse imaging of a 1-cm-wide vascular network during quail embryo development for over 24 hours, visualizing the movement of over 4.0×10^5 vascular endothelial cells and quantitatively analyzing their dynamics. Our results demonstrate the potential of this technique in accelerating production of comprehensive reference maps of all cells in organisms and tissues, which contributes to understanding developmental processes, brain functions, and pathogenesis of disease, as well as high-throughput quality check of tissues used for transplantation medicine.

MAIN TEXT

Introduction

Recently, life sciences have focused on comprehending the working principles of multicellular systems, spanning from basic biology to medical applications (1–5). Multicellular systems are generally complex, comprising heterogeneous cells rather than homogeneous assemblies. To understand the mechanism by which numerous cells cooperate to express the function of the entire system, it is ideal to observe all individual components within the system simultaneously during the time span of a whole phenomenon. In particular, in scenarios where a small fraction of cells in a large multicellular system may influence the fate of the population, or when distant cells and tissues operate synchronously, deducing the entire system from observations of sub-populations becomes challenging. Therefore, the trans-scale measurement of collective dynamics of all individual cells that constitute the system of interest is desired.

In response to this demand, researchers have recently reported the development of imaging methods with large field-of-view (FOV) (6–11). Whereas most of these methods are focused

on observing brain activity in neuroscience using two-photon excited fluorescence (7–10), our efforts have been dedicated to developing techniques as versatile tools for studying multicellular systems science and developmental biology. In our previous work, we proposed a fluorescence imaging system for the visible wavelength region, capable of spatially resolving individual cells within a centimeter FOV, which we named AMATERAS-1 (A Multi-scale/modal Analytical Tool for Every Rare Activity in Singularity), enabling simultaneous observation of dynamics in the range of 10^5–10^6 cells (11). Additionally, we successfully detected less than 1% of cells with unique roles in multicellular systems and revealed how these rare cells trigger a drastic transition from unicellular to multicellular behavior in *Dictyostelium discoideum* (12). However, the imaging system had a numerical aperture (NA) of 0.12, which is insufficient for realizing volumetric observation owing to its broad depth of field (DOF). Overcoming this limitation and enabling volumetric imaging for diverse three-dimensional (3D) tissues and small organisms has been a significant challenge.

In this study, we developed AMATERAS-2, a volumetric optical imaging system with approximately 15 × 10 mm^2 FOV, equivalent to that of AMATERAS-1 (11). The key component for the enhancement is the giant 2× lens system with an NA of 0.25, which offers improved 3D spatial resolution and higher sensitivity. By incorporating novel methodologies of optical sectioning and computational sectioning, we successfully added volumetric imaging capabilities. The effectiveness of these advancements was demonstrated in imaging 1.5-mm-thick brain section blocks and conducting a 25-h time-lapse observation of vascular endothelial cells during quail embryogenesis, allowing us to trace the spatiotemporal dynamics of approximately 4.0×10^5 cells in three dimensions.

RESULT

Optical configuration and performance

AMATERAS-1 utilized a telecentric macro lens with 2× magnification, thus allowing dynamic observation in the centimeter-FOV with subcellular resolution (11). Despite its efficacy in biological studies, its low NA (0.12) limits both its spatial resolution in the *z*-direction, and system brightness. To overcome these constraints and expand the possibilities for observing cell

dynamics in tissues and embryos, we developed a giant lens system with a higher NA, consisting of a pair of objective and tube lenses. The objective lens is composed of 12 optical elements in 7 groups, while the tube lens is composed of 9 lenses in 6 groups (Fig. 1A). Both lenses are infinity-corrected with NAs of 0.25 for the objective and 0.125 for the tube lens, and have a field number of 44 mm (diameter) suitable for large-area image sensors. They are effectively aberration-corrected to the diffraction limit or lower in the visible wavelength range of 436–656 nm. The objective lens and tube lens have sizes of 144 mm × 310 mm and 170 mm × 345 mm, respectively (Fig. 1B). The objective and tube lenses exhibit zero vignetting, enabling observation of peripheral areas of the FOV with high brightness.

As the NA of AMATERAS-2 is 0.25, more than double that of AMATERAS-1 (0.12), our system in principle achieves over twice the spatial resolution in the transverse (*xy*) direction, more than four times the resolution in the longitudinal (*z*) direction, and over four times the brightness of AMATERAS-1.

Using this new lens system, we constructed a wide-field epi-illumination fluorescence imaging system, termed AMATERAS-2w, with a magnification of 2×, an NA of 0.25, and a field number of 44 mm (Fig. 1C, Materials and Methods). We utilized either a 120-megapixel CMOS camera or a 250-megapixel CMOS camera, depending on the research purpose. Both the cameras have an approximately 35 mm diagonal, thus providing an observation FOV of 17.8 mm and 17.4 mm diagonal at 2× magnification, respectively. The pixel sizes for these cameras are 2.2 and 1.5 μm, with sampling intervals of 1.1 and 0.75 μm at 2× magnification, respectively.

We installed a high-brightness LED light sources for fluorescence excitation, directing it into the objective lens through a custom-made long-pass dichroic mirror designed for GFP imaging with a cut-off wavelength of 497 nm. To ensure uniform illumination across the entire FOV, we employed a lens-let array pair. Additionally, we incorporated a 2-inch band-pass fluorescence filter between the tube lens and the camera.

We experimentally obtained the optical point spread function (PSF) using green fluorescent beads (center wavelength: 515 nm) with a 0.2-μm diameter, employing both the 120-megapixel

CMOS camera (Fig. 2A) and the 250-megapixel CMOS camera (Fig. 2B). The left panels in Figs. 2A and B display the PSFs in the *xy* and *xz* planes, respectively. The single-point spatial resolution was evaluated by the full-width of half-maximum (FWHM) of the line profiles determined through Gaussian-function fit. The transverse resolutions (*xy*-direction) obtained with the 120- and 250-megapixel cameras were 1.24 ± 0.12 (N = 100) and 1.12 ± 0.072 (N = 100) (Figs. 2A-B, right top), both of which are slightly downgraded from the theoretical FWHM, 1.05 µm, given by 0.51 λ_{em}/NA (λ_{em} = 515 nm, NA = 0.25) (13,14). This can be attributed to the coarse sampling interval (1.1 µm and 0.75 µm, respectively). In particular, in the 120-megapixel case, the apparent single-point resolution varies depending on the relative position of the bead within the pixel (Figs. S1A-B). The coarse sampling also introduces uncertainty in the estimated position of the bead's center coordinate (Fig. S1E). Although this may pose some challenges in quantitatively evaluating fine shapes in cells, it is not a practical issue in imaging at cell resolution. By contrast, the 250-megapixel camera provides a nearly constant resolution (Figs. S1C-D). Thus, the 250-megapixel camera is suitable when high-resolution images are required, whereas the 120-megapixel camera is suitable for other cases where increasing the number of photons per pixel or suppressing data size is necessary.

In the depth direction (*z*-direction), we evaluated the DOF by fitting Gaussian curves to the line profiles (Figs. 2A-B, right bottom). The DOF was measured to be 15.6 ± 1.3 (N = 100) and 14.8 ± 1.1 (N = 100) for the 120- and 250-megapixel cameras, respectively. This difference in DOF is attributed to the distinct pixel sizes of the cameras (15). The DOF value for the 250-megapixel camera was found close to the theoretical FWHM, 14.3 µm, given by 1.78 λ_{em}/NA^2 (λ_{em} = 515 nm, NA = 0.25) (14).

The spatial resolution in the transverse direction has been significantly improved, approximately two times compared with that of AMATERAS-1. Figures 2C and D display fluorescence images of cardiomyocytes derived from human induced pluripotent stem cells (hiPSCs) stained with Rhodamine phalloidin (C) across the entire FOV and (D) within a central local region indicated by a magenta square in (C). These images were captured using the 250-megapixel camera, and the FOV size was 14.7 × 9.4 mm^2. For comparison, Fig. 2E shows an

143 image of the same area observed with AMATERAS-1. Evidently, AMATERAS-2w delivers
144 more detailed images with finer spatial structures. This is further confirmed by the line profiles
145 depicted in Fig. 2F, where the filamentous actin stained with Rhodamine exhibits a sharper
146 spatial resolution with AMATERAS-2w. This result indicated the capability of observing
147 subcellular structures, such as myofibrils, in cell sheets with a large area, such as artificial
148 myocardial sheets, which would enable us to simultaneously investigate microscale structures
149 and macroscale multicellular dynamics.

150 **Spinning pinhole-array disk provides optical sectioning capability in wide-FOV**

151 This imaging system utilizes wide-field illumination and detection, which currently lacks the
152 capability to selectively acquire images of specific *z*-planes for volumetric imaging. To extend
153 the system's applicability, we developed two methods to enable the volumetric imaging, namely,
154 optical sectioning and computational sectioning.

155 For optical sectioning, various options of optical techniques exist for achieving 3D fluorescence
156 imaging with a large FOV in the visible wavelength region. These include scanning confocal
157 microscopy (6,13), light-sheet microscopy (4,16), light-field microscopy (17), two-photon
158 excitation microscopy (7-10,18), and spatiotemporal focusing (19). Among these options, we
159 selected the confocal imaging method for this study. This is because the light-sheet microscopy
160 struggles with uniform illumination over the centimeter scale FOV of AMATERAS (16,20),
161 and the light-field microscopy involves a trade-off between spatial resolution and the ability to
162 resolve three dimensions, which is incompatible with the AMATERAS's concept (21). In
163 addition, two-photon excitation microscopy, including that using spatiotemporal focusing, is
164 crucial for deep tissue imaging, but still requires further innovations in pulsed laser power and
165 scanning methods to be effectively applied to the wide FOV of AMATERAS.

166 We considered the confocal method to be the most compatible with our imaging system.
167 Considering the vast FOV, we adopted the multipoint-scanning confocal system. The
168 commonly used method involving a combination of a microlens array and a pinhole array disk
169 (22) could not be employed in AMATERAS owing to the large NA of the tube lens (NA =
170 0.125) compared with that of standard microscopes. Matching the NA requires shortening the

distance between the two disks or enlarging the microlenses. However, shortening the inter-disk distance leads to a loss of space for inserting a dichroic mirror, and enlarging the microlenses reduces the number of foci. While confocal reflection (non-fluorescence) microscopy does not require a beam splitter, allowing for close microlens-pinhole spacing (23), the confocal fluorescence microscopy requires a beam splitter due to the essential separation of fluorescence and excitation light. Therefore, designing microlens-pinhole arrays suitable for AMATERAS-2 presents a significant challenge. This challenge can be circumvented by using an optical configuration where excitation light and fluorescence pass through synchronized pinhole arrays on separate paths, as initially proposed in the early development of multipoint confocal microscopy (24). However, this solution would require duplicating the optics of the giant lens, which is currently unfeasible. Moreover, even if possible, the added complexity of the system would render this approach impractical.

To address this challenge, we opted to use pinhole arrays without microlenses, which is rather a more traditional configuration of multipoint confocal microscopy (13,25,26). Although this method is less light-efficient compared with the one using microlenses, it aligns well with our imaging system's high NA and low magnification. Here, we designed the pinhole array disk for fluorescence imaging in green (*e.g.*, GFP, YFP) and red (*e.g.* RFP, mCherry) wavelengths. Commercial confocal systems using pinhole-array disks typically feature large pinhole sizes (*e.g.,* 50 μm) and wide spacing between pinholes (*e.g.,* 200 μm), designed for general microscopes. For AMATERAS-2, however, with its 2× magnification and NA of 0.25, the pinhole size must be much smaller. The diameters of the Airy disk for green and red wavelengths are about 5 μm and 6 μm, respectively, at the focal plane of the tube lens (NA = 0.125). As a prototype, we set the pinhole size to 6 μm (Fig. 3A), matching the Airy disk diameter for red wavelength. A more detailed discussion on the impact of pinhole diameter dependence on 3D resolution is available in the Supplementary File (Note 1, Fig. S2). The pinhole spacing was set as 24 μm, striking a balance between throughput and crosstalk (Fig. 3A). To implement this, we custom-made a pinhole-array disk and incorporated it into a rotary machine (CrestOptics, Rome, Italy).

We positioned the pinhole array disk at the image plane of the tube lens and constructed a relay lens system to transfer the plane to the camera. This particular configuration, termed AMATERAS-2c, is illustrated in Fig. 3B (Materials and Methods). To split the light paths of fluorescence excitation light, we placed a short-pass dichroic mirror beneath the disk. For fluorescence excitation, we used a high-brightness LED with a center wavelength of 470 nm, the same as in the wide-field imaging system (Fig. 1C). The relay lens consisted of a telecentric macro lens with 1× magnification, and a 2-inch band-pass fluorescent filter was positioned at the entrance of the macro lens. If necessary, the relay lens can be replaced by a 2× magnification lens to switch the total magnification from 2× to 4×, based on resolution requirements.

Fluorescence images of 0.5 μm fluorescent beads were observed with and without the pinhole-array disk, where fluorescent beads were three-dimensionally dispersed in an agarose gel slab (Fig. 3C). The presence of the pinhole-array disk dramatically suppressed background light from outside the focal plane. This verified that optical sectioning can be achieved by the pinhole-array disk. The variations in the 3D PSF with and without the pinhole-array disk are detailed in the Supplementary File (Fig. S3). Typical 3D PSF was obtained with the fluorescence beads with the relay lens of (D) 1× and (E) 2× magnifications (Figs. 3D and E). As NA of the 1× relay lens (NA = 0.079) is lower than that of the tube lens (NA = 0.125), the transverse spatial resolution (Fig. 3D, right top) is degraded compared to the one obtained by the wide-field configuration without the relay lens (Figs. 2A and B, Note 1). By contrast, the 2× relay lens (NA = 0.12) almost matches with the tube lens, and the reduction in the transverse spatial resolution is relatively small (Fig. 3E). As for the longitudinal resolution, the FWHM of the PSF was approximately 16 μm with a 1× relay lens and approximately 14 μm with a 2× relay lens, both values significantly exceeding the ideal value about 9.5 μm (Note 1). These discrepancies are attributed to the relatively loose focusing of the excitation light and the non-negligible size of the pinhole.

Computational sectioning provides pseudo-depth-resolved imaging capability

In addition to optical sectioning, we developed a computational sectioning method to separate images of the focal plane and out-of-focal planes. During measurement, a *z*-stack is acquired in

227 the wide-field imaging configuration (Fig. 1C) by scanning the focal position in the *z*-direction
228 and capturing images at each step. The raw image in a 3D volume results from the superposition
229 of in-focus and out-of-focus plane images. We estimated the contribution from out-of-focus
230 planes as the baseline by iteratively applying low-pass filtering under the assumption that the
231 image's spatial frequency in the focal plane is higher than that in out-of-focus planes. The cut-
232 off frequency of the low-pass filter was optimized using the principles of independent
233 component analysis (Materials and Methods, Note 2, Fig. S4-S5).

234 To demonstrate computational sectioning, we observed myocardial organoids derived from
235 hiPSCs (27). This 3D dome structure of a cavity chamber is extensively studied in
236 developmental biology and regenerative medicine as a model for human myocardial tissue
237 development (28,29). We fabricated a large area of organoids across the entire FOV, chemically
238 fixed and immunostained them for cardiac troponin T (cTnT) with Alexa488, and stained the
239 nuclei with Hoechst33342 (Materials and Methods). The *z*-stack was obtained within a *z*-range
240 involving the organoids (approximately 250 μm) with 4-μm intervals. Figures 4A and B display
241 two-color overlaid images of the island-formed organoids across the entire FOV, without and
242 with computational sectioning, respectively (both are maximum-intensity projection (MIP)
243 images of the *z*-stacks). Figures 4C and D present images of six layers in the *z*-direction of the
244 yellow square region of Figs. 4A and B, before and after computational sectioning, respectively.
245 After the sectioning, the distribution of cTnT and nuclei in each *z*-layer is clearly visualized
246 (Fig. 4D): The island areas are composed of multilayered cells, and the inter-island spaces are
247 covered with a single layer of cells, as shown in Fig. 4D, z = 20 μm. A 3D isosurface
248 representation (Fig. 4E) shows that the hollow oval structure is formed by a thin layer of cTnT-
249 positive cells (cardiomyocytes) whereas the underlying cell layer is composed of cTnT-negative
250 cells, consistent with previous literature (27). This demonstration validates the technique for
251 wide-field imaging. Video files of Figs. 4C–E are available in the Supplementary files (Movies
252 S1 and S2).

253 In principle, the signal component can be extracted as long as the signal intensity (in-focus
254 component) is significantly higher than the statistical noise of the background intensity (out-of-

focus component). This method is effective in cellular imaging when fluorescent molecules are localized within the cell, like in the nucleus, or when they exhibit a filament-like structure, thereby enabling cell recognition and dynamic tracking. It relies on the spatial frequency of the fluorescence image in the focal plane being uniform and clearly higher than that outside the focal plane.

Observing a 1.2-cm wide and 1.5-mm thick volume of mouse brain section

To demonstrate the potential for brain imaging, we performed imaging of a 1.5-mm thick mouse brain section in the coronal plane (Fig. 5A). The brain was chemically cleared using CUBIC (30,31), and the cell nuclei were stained with SYTOX-Green (Materials and Methods). The 1× relay lens was primarily employed (total magnification = 2×) to cover the coronal plane in the FOV. Each layer's exposure time was 1 s, and a total of 378 layers were acquired to cover the entire 1.5-mm-thick volume in steps of 4 μm in the *z*-direction. Optical and computational sectioning were both applied. Figure 5B shows a fluorescence image at a single *z*-layer (z = 700 μm), revealing the 12 mm × 8 mm wide section with single cell resolution. Figure 5C displays enlarged views of the *xy*-plane (coronal plane) in the dotted square region in Fig. 5B, along with *xz* (transverse plane) and *yz* (sagittal plane) cross sections, essentially demonstrating successful *z*-direction sectioning. Figure 5D shows a 3D representation of the same volume of raw data obtained by optical sectioning alone, prior to computational sectioning. However, owing to intense background light overlapping, individual cells are challenging to distinguish, particularly in regions of high cell density. By utilizing computational sectioning to eliminate background light, clear images were obtained even in areas with strong background light. Supplementary files contain videos of the *z*-scan for the entire FOV and local regions (Movies S3 and S4).

Figure 5C visualizes the characteristic 3D structures of several regions, including hippocampal dentate gyrus, medial habenula, and choroid plexus, which are known to be associated with memory formation (32), depression (33), and regulation of cerebrospinal fluid (34), respectively. Close-up views of the hippocampal region (indicated with the dashed square in Fig. 5B) in the *xy* and *xz* planes are shown in Figs. 5E and F, respectively. A comparison of the images at 2×

283 and 4× magnification in Figs. 5E and F reveals that the higher magnification (4×) allows for
284 improved spatial resolution and separation of individual cells in both the *xy* and *xz* planes.

285 For cell detection in the 3D imaging data of the mouse brain section, we used a recently
286 developed interactive platform for cell detection and tracking, called ELEPHANT (Efficient
287 LEarning using sParse Human Annotations for Nuclear Tracking) (35). This platform
288 seamlessly integrates manual annotation with deep learning and allows for result proofreading
289 (Materials and Methods). Using this advanced image analysis technique, cell nuclei were
290 detected within the 3D volume. Figure 5G illustrates the cell detection results on specific *xy*
291 and *xz* planes within the cortex. As the cell density in the cortex is relatively low, the ellipsoid-
292 shaped nuclei image does not overlap with neighboring cells, resulting in the successful
293 detection of nearly all cells (as clearly shown in the *z*-scan video, Movie S5). The precision and
294 recall of the cell detection were estimated to be 99.4 % and 97.6 %, respectively (Materials and
295 Methods). Based on these results, the cell density in the cortex was calculated to be 1.18×10^5
296 cells/mm^3, which closely matches previous reports (36). This technique was also applied to two
297 other brain regions, the medial habenula and choroid plexus (Figs 5H-I). In these regions, cell
298 density is higher than in the cortex and the signal-to-noise ratio is lower due to strong
299 background intensity, making it difficult for traditional methods to detect cells accurately.
300 However, with the assistance of ELEPHANT, we successfully detected the majority of cells.

301 **Dynamics of over a 4.0 x 10^5 cells were captured over 24-hours development of a quail**
302 **embryo**

303 We employed the imaging methods described for a time-lapse observation of cell migration
304 during quail development. The non-confocal optical configuration (AMATERAS-2w, Fig. 1C)
305 and utilizing computational sectioning alone were sufficient for this 250-µm thick sample. We
306 used a tie1:H2B-eYFP transgenic quail embryo (37) in which enhanced yellow fluorescent
307 protein (eYFP) visualizes the nuclei of vascular endothelial cells (Materials and Methods). The
308 embryo was cultured *ex ovo* on a 35 mm glass-bottom dish (Fig. 6A). Time-lapse fluorescence
309 imaging began at 36 h (HH10) after the start of egg incubation and captured eYFP signals in
310 the developing embryo over 24 h. For 3D imaging, we acquired *z*-stacks every 7.5 min, with

311 each *z*-stack containing 21 layers spaced 12 μm apart. This resulted in a total of 4200 image
312 layers and 200 time-points, with a data size of approximately 500 GB. During the time-lapse
313 observation, we stabilized the relative distance between the lens and the sample using a self-
314 developed autofocus system (Materials and Methods).

315 Representative images of cell distribution based on the nuclear eYFP signals at four time-points
316 (t = 0, 8, 16, and 24 h) are shown in Figs. 6B and C. These images were reconstructed using the
317 HSB color model to represent the 3D distribution after the baseline was removed by
318 computational sectioning (Fig. S6). The brightness indicates the intensity of the MIP image in
319 the *z*-direction, whereas the hue represents the *z*-position with the maximum value in the MIP
320 process (Materials and Methods). As observed in Figs. 6B and C, the cell nuclei distribution
321 undergoes significant changes over time, thus resulting in the formation of organs such as the
322 ventral aortae, heart, and dorsal aortae (t = 24 h, Fig. 6C). The heart region appears blurred
323 owing to its oscillating shape caused by beating. Supplementary files include videos of the
324 HSB-color images in the entire FOV and magnified local regions (Movies S6–S8). Figure 6D
325 shows enlarged views of the ventral aortae (indicated by the left dashed square in Fig. 6C) at
326 the four time-points. Additionally, a 3D isosurface of the *z*-stack of the dorsal aorta region (the
327 right dashed square in Fig. 6C) was calculated (Fig. 6E, and Movie S9), clearly showing the
328 developmental process of the two tube structures of the dorsal aortae (38). Note that the upper
329 vessel wall is partially missing in the second half of the movie because the fluorescent image
330 was disturbed by the blood flow that began around t = 15 h.

331 At the current spatiotemporal resolution, we successfully traced the movement of individual
332 cells. Segmentation of cell nuclei allowed us to detect approximately 4.5×10^6 cells across all
333 200 frames, and by linking cells in close proximity over consecutive frames, we tracked about
334 4.0×10^5 cells. Figures 6F and G show cellular movement along with a feature parameter related
335 to cell movement at t = 8 h and 16 h. Both left panels are magnified views of the square regions
336 in the right panels, with trajectories drawn on MIP images. By analyzing the cell segmentation
337 and tracking results, various feature parameters related to cell nucleus morphology and
338 dynamics were computed, including nuclear size, brightness, aspect ratio, velocity, acceleration,

339 mean square displacement, and meandering index (39,40). Here, we used the meandering index,
340 a measure representing the straightness of cellular movement, to color the trajectories in Figs.
341 6F and G with the rainbow color table. We found that the distribution of high meandering index
342 at t = 8 h and 16 h was significantly changed. Further detailed analysis and biological
343 interpretation employing the cell-tracking results will be discussed in a future paper.

344 **Discussion**

345 In this study, we presented AMATERAS-2w, a large FOV fluorescence imaging system, along
346 with its variant AMATERAS-2c. The system is built around a newly designed giant lens with
347 an NA of 0.25, magnification of 2×, and field number of 44 mm. This innovative lens
348 configuration allows for imaging with an impressive spatial resolution of approximately 1.1 μm
349 within a centimeter-scale FOV (15 × 10 mm^2). Notably, this FOV-to-spatial resolution ratio
350 surpasses those of previously reported large-FOV imaging methods. The key metric "optical
351 invariant", derived from the product of NA and FOV, has a value of 2.75 (Materials and
352 Methods, 41), thus indicating excellent performance of the lens system. Furthermore, the
353 "space-bandwidth product", which signifies the FOV to spatial resolution ratio achieved under
354 real measurement conditions (considering image sensor size and wavelength), reaches 4.3×10^8
355 (Materials and Methods, 42). Both of these metrics significantly outperform those reported in
356 earlier studies on large FOV imaging methods (6–10,41). Although these metrics are essential
357 indicators of our system's performance, they do not solely determine its superiority over other
358 large-FOV imaging systems. Variations in biological targets and additional optical performance
359 measures (such as frame rate and imaging depth) must also be considered. Our primary focus
360 in designing this system was to expand the FOV, *i.e.*, maximize the number of observable cells
361 at any instant, even at the cost of intracellular spatial resolution. Thus, in this aspect, our system
362 excels as an instrument for such purposes.

363 The spatial resolution (FWHM) of AMATERAS-2w and -2c was measured to be approximately
364 1.1–1.8 μm in the transverse direction (xy) and 13–16 μm in the longitudinal direction (z)
365 through PSF measurements (Figs. 2A, 2B, 3D, and 3E). These values represent a significant
366 enhancement compared with the previous AMATERAS version (2.3 and 64 μm, respectively)

367 (11). The improved transverse resolution enables clearer visualization of intracellular
368 filamentous structures (Fig. 2F). Moreover, the refinement in longitudinal resolution was more
369 than four times greater, thus demonstrating that the expected effect was achieved with more
370 than double NA. Depending on the object of observation, it may be debatable whether this
371 anisotropic spatial resolution elongated along the optical axis qualifies "cellular resolution".
372 Although this may be insufficient to resolve dense cell populations, it proves adequate for cells
373 with only stained nuclei or those sparsely distributed, as observed in Figs. 5F-I, and 6E. Using
374 modern cell detection methods compatible with 3D big data, such as ELEPHANT employed in
375 this study (35), we can achieve accurate cell detection, counting and tracking to some extent,
376 even without clear spatial separation in three dimensions. It goes without saying that the higher
377 spatial resolution in raw image data would enhance the performance of subsequent image
378 analysis. The next step in optical development involves further enhancing the NA of the lens
379 system, including the relay lens, to further improve volumetric resolution and expand the range
380 of observable biological objects.

381 We successfully achieved volumetric imaging of a 1.5-mm-thick mouse brain coronal section
382 using the multipoint-scanning confocal imaging method, along with computational sectioning
383 and tissue-clearing (Fig. 5). This thickness corresponds to about one-tenth of the whole brain.
384 The exposure time per image was 1 s, and data acquisition took less than 10 min. The ultimate
385 goal is to apply this approach to enable whole-brain imaging. Unlike previous methods such as
386 light-sheet imaging (30) and block-face serial microscopy tomography (43), which require half
387 a day or more for whole-brain data acquisition owing to tiling images from a narrow FOV, our
388 method can significantly reduce the acquisition time when extended to the whole brain. This
389 feature is effective not only for the brain imaging but also for imaging of other organs and whole
390 body of an organism. We also plan to apply it to live imaging of highly transparent tissues such
391 as zebrafish (44) and organoids (45). Nevertheless, as the thickness increases, challenges such
392 as increased background light and larger spherical aberration arise, thus resulting in weaker
393 focal plane images. To address these issues and realize whole-brain imaging, we propose the
394 incorporation of a mechanism for compensating spherical aberrations in the future. Additionally,
395 we aim to improve the pinhole array pattern design and light source intensity to enhance

transmittance and increase fluorescence intensity from samples, broadening the scope of applications.

We have shown that AMATERAS-2 can perform time-lapse observation of the centimeter-sized vascular networks in the quail embryo. It is a promising tool for understanding the multicellular behavior, especially the mechanisms of tissue formation during development (1-3). In regard to the quail embryo's case, the data obtained here are the first demonstration of the dynamics of the extensive organization of the vascular network throughout the quail embryo at the single-cell level. Conventional methods of research employing traditional microscopy have selected a limited area for observation and thus had a difficulty in determining the distribution and synchronicity of cellular dynamics across the entire system. By analyzing such a huge four-dimensional data (*xyz* and *t*), we can gain insight into when and where each organ is formed, in what order, and in what interrelationships. In addition, employing this method allows us to break away from the conventional hypothesis-driven research manner and obtain new findings in a data-driven manner. This advantage can be realized not only for quail embryo but also for a variety of other species undergoing widespread and dynamic cellular events, making it a powerful tool in the study of multicellular organisms, especially in the study of tissue formation.

To further advance multicellular systems research, information on individual cell states is required in addition to cellular dynamics, therefore multiplex measurement is an essential technological challenge. Although most of the observations presented in this paper were made with monochromatic fluorescence imaging, multiplex imaging will lead to a more profound understanding if information on the distribution of cellular states can also be obtained by employing multiple fluorescent probes. This requires technological upgrades in optical filters and light sources for multicolor imaging. In addition, spatial transcriptomics has been rapidly developing in recent years and has become one of the most crucial tools for multicellular system study (5). In the near future, dynamics imaging and spatial transcriptomics for the same sample will be a very important technological integration to advance an integrative understanding of self-organization in tissue formation. Rather than simply using AMATERAS sequentially with existing spatial transcriptomics, it could be employed as an optical detection system for spatial

transcriptomics to achieve extremely high throughput in the same wide FOV of cellular dynamics imaging.

Finally, let us discuss a practical challenge we encountered with our instrument, primarily related to the handling of extensive image data. In our studies, the raw data for 3D imaging of the mouse brain section and time-lapse 3D imaging of the quail embryo amounted to approximately 100 and 500 GB, respectively. However, after multiple image processing and analysis steps, a single experimental measurement resulted in several terabyte of image data. Managing such vast data proves challenging for standard computers in terms of both software and hardware capabilities. To address software limitations, we opted not to employ commercial software for data analysis. Instead, we utilized our originally developed programs, implementing certain optimizations to reduce analysis time, minimize write/read cycles, and prevent memory overflows. As for hardware, we established a data server with petabyte storage, thereby enabling efficient data sharing among collaborators from diverse research institutions physically distant from one another. The existence of this infrastructure considerably facilitated the smooth progress of collaborative research within this study. Considering the increasing significance of handling image big data, we expect methodologies for image computation to become even more critical in the future. Ideally, a comprehensive system should be developed, encompassing not only data storage and sharing but also an integrated analysis solution in the cloud. We would like to actively promote the development of such a system, essentially encompassing advancements in imaging techniques and data-handling strategies.

MATERIALS AND METHODS

Wide-field imaging system (AMATERAS-2w) configuration

We aimed for AMATERAS to achieve a larger FOV-to-resolution ratio than conventional microscopes, which required a giant imaging lens system. We realized this design concept by collaborating with SIGMAKOKI CO., LTD. Inc. (Tokyo, Japan) to manufacture the giant objective and tube lenses as shown in Fig. 1. The characteristics of these lens are described in the main text. Designing such large lenses presents significant challenges in selecting optical glass materials compared to regular-sized lenses. Although there are over 200 types of optical glass available, our options are limited because the thickness or diameter of several types of glass may be unprocessable, or their transparency may degrade due to their size. Therefore, we iteratively explored the optimal design, considering the feasibility of material procurement and processing in conjunction with the optical design.

By combining these lenses, we constructed an imaging system with a 2× magnification, NA of 0.25, and a 44 mm field number. To facilitate both water-immersion and dry observation, we incorporated a glass plate whose thickness can be adjusted at the lens tip. The objective lens has a focal length of 120 mm, whereas its working distance is 14 mm owing to the presence of the attachment at the tip. The pupil positions of the objective lens and the tube lens are set externally to the lens bodies. This arrangement allows for the placement of a spatial filter or other devices at the pupil position, facilitating future enhancements in functionality.

For image acquisition, a 120-megapixel CMOS camera (VCC-120CXP1M, CIS, Tokyo, Japan) and a 250-megapixel CMOS camera (VCC-250CXP1M, CIS, Tokyo, Japan) were used, out of which we selected one depending on research purpose. Both the cameras have a chip size of 35 mm (diagonal). The pixel sizes of these two cameras are 2.2 μm and 1.5 μm, respectively. The sampling intervals are 1.1 μm and 0.75 μm at 2× magnification. Image data captured by the CMOS cameras are loaded into a workstation via a CoaXpress frame grabber board (APX-3664G3, Aval Data, Tokyo, Japan). After the imaging experiments, they were transferred to a network server with large storage capacity for long-term storage and data sharing among project members.

By use of the lens system and CMOS cameras, a wide-field epi-illumination fluorescence imaging system was constructed. The imaging system chassis was designed to accommodate both inverted and upright microscope geometries. For this study, all experiments were conducted using the inverted microscope arrangement. Epi-illumination was achieved using a high-brightness LED sources (SOLIS-470C and SOLIS-385C, Thorlabs, Newton, NJ), with an excitation filter (#87-800, Edmund Optics, Barrington, NJ) placed immediately after it. The illumination light was homogenized using a pair of lenslet arrays and projected onto the sample surface. Additionally, a similar LED light source (SOLIS-525C, Thorlabs, Newton, NJ) with an illumination homogenizer was also mounted as transmitted illumination light for bright-field observation. To split the light path, we used a custom-made long-pass dichroic mirror measuring 158 mm × 120 mm × 10 mm (BK7), which was designed for fluorescence imaging of GFP with a cut-off wavelength of 497 nm. A fluorescent filter (#86-992, Edmund Optics, Barrington, NJ) was positioned in front of the camera, which was firmly attached to the imaging lens using an F-mount.

The sample stage comprises a three-axis translational movable stage and a two-axis tilt stage. Only the *z*-axis stage is motorized, utilizing an electric actuator (SOM-C13E, SIGMAKOKI CO., LTD., Tokyo, Japan). For time-lapse observation under controlled conditions, we mounted a stage-top incubator (SV-141A, BLAST, Kawasaki, Japan) on the five-axis stage, providing a stable environment at 37 °C with CO_2 control. To ensure precise measurements, we enclosed the entire sample space within a dark box, shielding it from external light and temperature fluctuations.

Multipoint confocal system (AMATERAS-2c) configuration

In the multipoint confocal imaging system, we utilized a custom-made pinhole array disk with specific dimensions (pinhole size: 6 μm, spacing: 24 μm). This disk was mounted on a high-speed rotating machine (CrestOptics, Rome, Italy) and placed precisely on the image plane of the imaging lens. Alignment throughout the FOV was ensured using a translation stage (XR25P/M, Thorlabs, Newton, NJ) and tilt stage (AIS-1016B, SIGMAKOKI CO., LTD., Tokyo, Japan) to adjust height and tilt. Beneath the disk, we positioned a short-pass dichroic mirror

501 (DMSP490L, Edmund Optics, Barrington, NJ) to allow excitation light to be incident from
502 below. The excitation light source included a high-brightness LED (SOLIS-470C, Thorlabs,
503 Newton, NJ), an excitation filter (#87-800, Edmund Optics, Barrington, NJ), and a pair of
504 lenslet arrays (#63-231, Edmund Optics, Barrington, NJ), together with a 75-mm lens (f = 200
505 mm, LA1353-A, Thorlabs, Newton, NJ) to ensure uniform illumination onto the disk. The
506 fluorescent image was reflected by the dichroic mirror, transmitted through a fluorescent filter
507 (#86-992, Edmund Optics), and projected onto a 120-megapixel camera using either a 1× or 2×
508 relay lens (LSTL10H-F and LSTL20H-F, Myutron, Tokyo, Japan). The relay lens and camera
509 were attached with an F-mount and secured on a three-axis translational stage (PT3/M, Thorlabs,
510 Newton, NJ). To adjust the focus, the stage for the optical axis direction was motorized using
511 an electric actuator (SOM-C25E, SIGMAKOKI CO., LTD., Tokyo, Japan).

512 **Measurement of 3D point spread functions**

513 To evaluate the optical performance of the imaging systems, the 3D point spread function was
514 measured using green fluorescent beads. Fluorescent beads with a 0.2 μm diameter (FluoSphere
515 F8811, Invitrogen, ThermoFisher Scientific, Waltham, MA) were employed in the evaluation
516 of AMATERAS-2w (Figs. 2A-B) and those with a 0.5 μm diameter (FluoSphere F8813,
517 Invitrogen, ThermoFisher Scientific, Waltham, MA) were employed in the evaluation of
518 AMATERAS-2c (Figs. 3D-E). The beads were dispersed three-dimensionally in agarose gel on
519 a glass-bottom dish, and *z*-stacks were obtained by moving the sample in the *z*-direction in 1 or
520 2 μm steps.

521 **Computational sectioning**

522 In wide-field fluorescence imaging of a 3D volume, the superimposition of a fluorescent image
523 from the focal plane and background light from outside the focal plane is a fundamental issue.
524 This problem is not limited to wide-field imaging but also arises in multipoint confocal imaging
525 of thick or high-density samples. To overcome this challenge, we employed computational
526 sectioning, an image processing technique aimed at removing the background light component.
527 Various algorithms have been proposed (46,47), and Leica microscopes' standard software
528 includes this functionality. In this study, we developed an original algorithm as a simple and

robust method for data analysis.

The critical step in our approach involves estimating the background light component at each layer of the *z*-stack data. To achieve this, we leverage the assumption that the background light exhibits a low spatial frequency, whereas the focal plane image demonstrates a high spatial frequency. Consequently, we employ an iterative low-pass filtering technique to estimate the background light component. Specifically, as shown in Figs. S6A and B, a two-dimensional (2D) low-pass filter is applied to the raw data ($f_0(x,y)$) to obtain a smooth surface ($L_0(x,y)$). To obtain $f_1(x,y)$, $f_0(x,y)$ and $L_0(x,y)$ are compared and the smaller one is chosen to $f_1(x,y)$ at every position (x,y), as expressed by Eq. (1).

$$f_j(x,y) = \min\left(f_{j-1}(x,y),\ L_{j-1}(x,y)\right) \tag{1}$$

where min(a,b) returns the smaller value of a and b. Next, the low-pass filter is applied to $f_1(x,y)$ to obtain $L_1(x,y)$; this process is repeated to make $L_j(x,y)$ closer to the baseline of the original image. The iteration stops when the standard deviation of the difference of $f_j(x,y)$ and $L_j(x,y)$ reaches a preset value (ε).

$$\sqrt{Var\left(f_j(x,y) - L_j(x,y)\right)} < \varepsilon \tag{2}$$

Among various methods available as 2D low-pass filters, we sequentially applied one-dimensional (1D) infinite impulse response (IIR) filter in two directions (x,y). This method is faster than other methods such as a 2D Fourier transform (48). This speed difference is especially significant when the number of pixels in an image is massive, as in the present case. We adopted the Butterworth type of the IIR low-pass filter.

When the focal plane is empty and there is a bright object in the background, the baseline estimation tends to be skewed by the intensity fluctuations of the background. To mitigate this, we applied a 3×3 moving average filter to the entire image as a pre-processing step before initiating the baseline estimation algorithm. A critical parameter in our algorithm is the cutoff frequency of the low-pass IIR filter. If the cutoff frequency is set too high, the focal plane

554 component would be included in the background; if it is set to low, background light would
555 remain in the focal plane. Thus, it is crucial to find an optimal middle ground for the cutoff
556 frequency. During this optimization, we did not account for cell size or optical system
557 performance. Indeed, we employed a user-friendly blind separation method based on
558 independent component analysis (ICA) to enhance usability (49). Similar to ICA, we assumed
559 that the fluorescence image in the focal plane deviates from the Gaussian (normal) distribution
560 and that the superposition of images from multiple planes, including both in-focus and out-of-
561 focus planes, results in a distribution closer to the Gaussian distribution. To quantify the non-
562 Gaussian nature of the distribution, we considered several measures, including kurtosis,
563 skewness, negentropy, and mutual information (49). Among these measures, we found
564 skewness to be the most robust metric for our image dataset and incorporated it into our
565 algorithm. The cutoff frequency was adjusted to maximize the skewness of the estimated in-
566 focus image. The optimization of the cut-off frequency was performed on a subset of the data
567 before applying it to the entire dataset. An example of the selection of non-Gaussianity measure
568 and the optimization of the cut-off frequency is found in the Supplementary File (Fig. S4-S5,
569 Note 2). The typical cut-off frequency was set at 0.06 in normalized frequency unit of 1/pixel,
570 and the value was applied across all data.

571 **Culture of hiPSCs and differentiation into cardiac organoid with cavity chamber**
572 **structure**

573 A hiPSC line 201B7 was routinely maintained as previously described (50) on iMatrix-511
574 (Matrixome, 89292) coated culture dish in StemFit medium (Ajinomoto, AK02N), and 10 μM
575 Y-27632 (Fujifilm Wako, 030-24021) was added for the first 24 h after passage. Four days
576 before inducing differentiation, hiPSCs were dissociated with TrypLE Select Enzyme (Thermo
577 Fisher Scientific, A1285901) and 1.9×10^5 cells were passed into iMatrix-511 coated 12 well
578 plate in StemFit medium supplemented with 10 μM Y-27632. After 24 h, the medium was
579 changed to StemFit without Y-27632 and was exchanged daily for 3 days. Differentiation was
580 initiated with the CDM3 medium (51) composed of RPMI-1640 with HEPES (Fujifilm Wako,
581 189-02145), 0.5 mg/ml human recombinant albumin (Sigma Aldrich, A9731) and 0.2 mg/ml L-
582 ascorbic acid 2-phosphate (Sigma Aldrich, A8960) supplemented with 3 μM CHIR99021

583 (Fujifilm Wako, 038-23101) for 48 h. On day 2 of differentiation, the medium was changed to
584 CDM3 supplemented with 5 μM IWP-2 (Fujifilm Wako, 034-24301). From day 4 to day 8, the
585 cells were cultured in CDM3 and the medium was changed every other day. From day 8, the
586 medium was changed to RPMI-1640 with HEPES supplemented with 2% B27 (Thermo Fisher
587 Scientific, 17504044) and was changed every other day. The cells were fixed in 4%
588 paraformaldehyde (PFA; Thermo Fisher Scientific, 43368) on day 15 for immunocytochemical
589 analysis.

590 **Immunocytochemical staining of cardiac organoid**

591 Cells were fixed with 4% PFA for 15 min at room temperature (RT ~23 °C), permeabilized with
592 0.2% Triton X-100 (Fujifilm Wako, 807423) for 20 min at RT and incubated with blocking
593 solution composed of D-PBS with 5% BSA and 10 % FBS for 30 min at RT. Subsequently, the
594 cells were incubated with primary antibody (1:200 rabbit IgG anti-cTnT, Bioss, bs-10648R) at
595 4 °C overnight. After washing three times, cells were incubated with secondary antibody (1:500
596 alexa488 conjugated goat IgG anti-rabbit IgG, Abcam, ab150077) for 2 h at RT. The cells were
597 washed three times in D-PBS with 1 μg/ml Hoechst33342 (Dojin, H342). Subsequently, the
598 cells were incubated with D-PBS and used for fluorescent observation.

599 **Color representation of the 3D image**

600 Figures 6B–D show the 3D positions of the cells using the HSB (also known as HSV) color
601 model. After applying the method described earlier to remove background light from the *z*-stack
602 image, we conducted a maximum value intensity projection along the *z*-direction. The *z*-
603 position of the maximum value at each *xy*-position was then recorded (Fig. S6C). The color
604 image was reconstructed by associating the brightness and hue of the HSB table with the value
605 of the maximum intensity and the maximum value position, respectively (Fig. S6D). For the
606 hue table, we assigned red to blue to *z*-layer numbers ranging from 0 (z = 0 μm) to 20 (z = 240
607 μm).

608 **Preparation of mouse brain section**

609 All animal care and handling procedures were conducted with approval from the Animal Care
610 and Use Committee of Osaka University (approval numbers R02-8-7). Our utmost efforts were

611 made to minimize the number of animals used. Experiments involved adult male C57BL/6J
612 mice (SLC, Shizuoka, Japan) aged between 2 and 3 mo. To ensure proper anesthesia, mice were
613 deeply anesthetized through intraperitoneal injection of an anesthetic cocktail containing 0.3
614 mg/kg medetomidine (Nippon Zenyaku Kogyo, Fukushima, Japan), 4 mg/kg midazolam
615 (Sandoz Pharma, Basel, Switzerland), and 5 mg/kg butorphanol (Meiji Seika Pharma, Tokyo,
616 Japan). Subsequently, anesthetized mice underwent transcardial perfusion with saline, followed
617 by 4% paraformaldehyde (Nacalai Tesque, Kyoto, Japan) dissolved in phosphate-buffered
618 saline (PBS). Brain tissues were then excised and immersed in a 4% paraformaldehyde solution
619 until further use. For tissue preparation, brain tissue blocks were sliced into 1.5-mm thick
620 coronal sections using a vibrating microtome (LinearSlicer Pro7N, Dosaka EM, Kyoto, Japan).
621 Subsequent staining and tissue clearing involved immersion of sections in CUBIC-L (Tokyo
622 Chemical Industry, Tokyo, Japan) for delipidation, SYTOX Green (Thermo Fisher Scientific,
623 Waltham, MA, USA) solution (1:5,000) diluted in 20% (vol/vol) DMSO in PBS for nuclear
624 staining, and CUBIC-R+(M) (Tokyo Chemical Industry, Tokyo, Japan) for refractive index
625 matching, following previously established methods (31,52). After clearing, tissue sections
626 were placed on glass bottom dishes and embedded in 2% (wt/vol) agarose gel prepared with
627 CUBIC-R+(M) for subsequent imaging analysis.

628 **Preparation of quail embryo**

629 Transgenic quail line, tie1:H2B-eYFP (37) was bred in quail breeding facility at Kyushu
630 University. Fertilized eggs were incubated at 38 °C. The staging of quail embryos was based on
631 the Hamburger and Hamilton stages of chicken embryos (53). The animal study was approved
632 by the Institutional Animal Care and Use Committee of Kyushu University (Authorization
633 number: A20-019). *Ex ovo* culture was performed as previously described (54). Black filter
634 paper was used instead of white filter paper to avoid fluorescence background.

635 **Autofocus in time-lapse imaging**

636 To address *z*-directional drift in the time-lapse observation of quail, we developed an original
637 autofocus method. During the intervals between fluorescence z-images, we acquired bright-
638 field *z*-stacks and analyzed the images to identify the most in-focus position. To achieve this,

639 we used a black ink marker located on the substrate edge as the autofocus target instead of the
640 variable sample itself. For evaluating the degree of in-focus, we applied a total variation (TV)
641 filter to the marker image and used the kurtosis of the filtered image as the focus score. The *z*-
642 position with the maximum focus score was identified as the in-focus location, thus signifying
643 the sharpest image of the marker edge. Although other filter types and statistical moments are
644 available options for the focus score (55), our preliminary experiments demonstrated the
645 suitability of the kurtosis of TV for the marker image. In the actual experiment, we acquired 15
646 images in 15 μm steps and plotted the focus scores against *z*-positions. Through quadratic
647 function fitting of the focus scores at three z-positions (including the *z*-position with the
648 maximum value and adjacent positions), we estimated the best in-focus position with an
649 accuracy of 1 μm.

650 **Deep-learning based cell detection for the mouse brain data**

651 Cell detection was conducted using ELEPHANT, a unified platform that facilitates manual
652 annotation, deep learning and proofreading of results within a single user-friendly GUI (35,56).
653 ELEPHANT serves as an extension to Mastodon (57), an open-source framework for large-
654 scale tracking deployed in Fiji, a widely used image-analysis software (58). ELEPHANT
655 supports incremental deep learning with sparse annotation, incorporating algorithms for
656 detecting cells in 3D and tracking them in time-lapse 3D image datasets. In this paper, we
657 utilized the cell detection function exclusively for analyzing 3D imaging data of mouse brain
658 section (Fig. 5G-I). The incremental learning approach allows cell detection models to be
659 trained progressively on a dataset that begins with sparse annotations and is continuously
660 enhanced through human proofreading. For visualization, image data were displayed using
661 BigDataViewer (59) on Mastodon, accessed via BigDataServer (60). This setup permits the
662 visualization of large-scale image data on client computers while maintaining the data on the
663 server. Deep learning capabilities were provided by the ELEPHANT server, enabling remote
664 GPU access. This setup allows non-experts to perform image analysis on big data using deep
665 learning, effectively overcoming typical challenges such as the need for large amounts of high-
666 quality training data, the absence of an interactive user interface, and limited access to
667 computing resources, including substantial storage and high-end GPUs (61,62). The server

computer used in this study is equipped with an Intel(R) Xeon(R) Gold 6132 CPU @ 2.60GHz, runs Ubuntu 20.04, and includes 384 GB DDR4 2,666 MT/s RAM, 2x NVIDIA Tesla V100-PCIE-32GB GPUs, and a network-attached Lustre parallel file system with over 2 PB of storage. The client computer features an Apple M1 Pro CPU, runs Sonoma 14.3, and has 16 GB of LPDDR5-6400 RAM and a 500 GB SSD.

In the analyses presented in this paper (Fig. 5G-I), cell detection models were trained for three regions, including the cortex. In each region, the detection model was refined by repeating the sequence (annotation, training, prediction and proofreading) five to seven times. By annotating approximately 100 cells in total, we were able to establish a model capable of detecting the vast majority of the cells. The training of the detection models was conducted on volumes of 256 × 256 x 16 voxels, which were prepared by preprocessing with a random flip in each dimension. During the label generation step, the center ratio was set to 0.4 and the background threshold was set to zero, meaning that only explicitly annotated voxels were used for training. In the prediction step, volumes cropped to dimensions of 700 × 700 × 100 around the target area were used as input. In the postprocessing step, a threshold for nucleus center probabilities was set to 0.5, and r_{min}, r_{max} and d_{sup} were set to 1 μm, 5 μm, and 3 μm respectively (see details about the parameters in 35).

To quantitatively evaluate the performance of cell detection, we calculated precision and recall, defined as TP/(TP+FP) and TP/(TP+FN), respectively, where TP stands for true-positive, FP for false-positive, and FN for false-negative. In the actual 3D data of the cortical region, the values of TP, FP, and FN were manually counted by comparing the detection results of cells (N ~ 640) within a defined volume of 310 × 170 × 100, one by one, with the actual images. As a result, we obtained a precision of 99.4 % and a recall of 97.6 %.

Cell segmentation and tracking for the quail embryo data

For the analysis of quail embryo data, cell detection, segmentation and tracking were performed using a custom-made program coded in Python. The observed 3D volume has a transverse area (xy) of more than 1 cm^2 and a height (z) of 240 μm, which is relatively thin in the z direction compared to the xy plane. The overlap of multiple vascular endothelial cells in the z direction

occurs with a very low probability. Therefore, to save computational costs and time, 2D cell detection was conducted on *z*-projected MIP images instead of full 3D cell detection. To avoid miss-detection of overlapping cells, we divided the *z*-stack data into three blocks along the z-axis and created MIP images for each block, on which 2D cell detection was performed on the MIP images. The resulting cell lists were compared to identify identical cells detected across multiple blocks. By recognizing double-detected cell pairs as identical, we updated the cell list accordingly. This process was applied to all double-detected cells, thus achieving effective cell detection in the 3D volume and enabling cell tracking throughout the observation period.

Evaluation of optical system with optical invariant and space-bandwidth product

We employed two indices to evaluate the lens system's scale range and compare it with previous research. The first index, the optical invariant, measures the lens system's performance and is obtained by multiplying the FOV radius and NA. The second index, the space-bandwidth product, considers the image sensor and wavelength while quantifying the ratio of actual resolution to FOV. These indices are calculated using the following simplified formulas, respectively (41).

$$I = \frac{NA \times FN}{2M} \qquad (3)$$

$$SBP = 8\left(\frac{R_{FOV}}{d_{xy}}\right)^2 \qquad (4)$$

where I, FN, M, SBP, R_{FOV}, and dxy denote optical invariant, field number, magnification, space-bandwidth product, FOV radius, and spatial resolution (FWHM).

716 **References**

717 1. Y. Sasai, Cytosystems dynamics in self-organization of tissue architecture. *Nature*. **493**,
718 318–326 (2013).

719 2. K. McDole, L. Guignard, F. Amat, A. Berger, G. Malandain, L. A. Royer, S. C. Turaga,
720 K. Branson, P. J. Keller, In Toto Imaging and Reconstruction of Post-Implantation
721 Mouse Development at the Single-Cell Level. *Cell.* **175**, 859-876.e33 (2018).

722 3. M. H. Dominguez, A. L. Krup, J. M. Muncie, B. G. Bruneau, Graded mesoderm
723 assembly governs cell fate and morphogenesis of the early mammalian heart. *Cell*. **186**,
724 479-496.e23 (2023).

725 4. H. R. Ueda, H. U. Dodt, P. Osten, M. N. Economo, J. Chandrashekar, P. J. Keller,
726 Whole-Brain Profiling of Cells and Circuits in Mammals by Tissue Clearing and Light-
727 Sheet Microscopy. *Neuron*. **106**, 369–387 (2020).

728 5. A. Rao, D. Barkley, G. S. França, I. Yanai, Exploring tissue architecture using spatial
729 transcriptomics. *Nature*. **596**, 211–220 (2021).

730 6. G. McConnell, J. Trägårdh, R. Amor, J. Dempster, E. Reid, W. B. Amos, A novel optical
731 microscope for imaging large embryos and tissue volumes with sub-cellular resolution
732 throughout. *Elife*. **5**, e18659 (2016).

733 7. N. J. Sofroniew, D. Flickinger, J. King, K. Svoboda, A large field of view two-photon
734 mesoscope with subcellular resolution for in vivo imaging. *Elife*. **5,** e14472 (2016).

735 8. J. Fan, J. Suo, J. Wu, H. Xie, Y. Shen, F. Chen, G. Wang, L. Cao, G. Jin, Q. He, T. Li, G.
736 Luan, L. Kong, Z. Zheng, Q. Dai, Video-rate imaging of biological dynamics at
737 centimetre scale and micrometre resolution. *Nat. Photonics*. **13**, 809–816 (2019).

738 9. K. Ota, Y. Oisi, T. Suzuki, M. Ikeda, Y. Ito, T. Ito, H. Uwamori, K. Kobayashi, M.
739 Kobayashi, M. Odagawa, C. Matsubara, Y. Kuroiwa, M. Horikoshi, J. Matsushita, H.
740 Hioki, M. Ohkura, J. Nakai, M. Oizumi, A. Miyawaki, T. Aonishi, T. Ode, M.
741 Murayama, Fast, cell-resolution, contiguous-wide two-photon imaging to reveal

functional network architectures across multi-modal cortical areas. *Neuron*. **109**, 1810-1824.e9 (2021).

10. C. H. Yu, J. N. Stirman, Y. Yu, R. Hira, S. L. Smith, Diesel2p mesoscope with dual independent scan engines for flexible capture of dynamics in distributed neural circuitry. *Nat. Commun.* **12**, 6639 (2021).

11. T. Ichimura, T. Kakizuka, K. Horikawa, K. Seiriki, A. Kasai, H. Hashimoto, K. Fujita, T. M. Watanabe, T. Nagai, Exploring rare cellular activity in more than one million cells by a transscale scope. *Sci. Rep.* **11**, 16539 (2021).

12. T. Kakizuka, Y. Hara, Y. Ohta, A. Mukai, A. Ichiraku, Y. Arai, T. Ichimura, T. Nagai, K. Horikawa, *bioRxiv*, doi:10.1101/2020.06.29.176891.

13. G. S. Kino, T. R. Corle, *Confocal Scanning Optical Microscopy and Related Imaging Systems 1st Edition* (Academic Press, Cambridge, MA, 1996).

14. T. Wilson, Resolution and optical sectioning in the confocal microscope. *J. Microsc.* **244**, 113–121 (2011).

15. H. Gross, F. Blechinger, and B. Achtner. *Handbook of Optical Systems, Volume 4: Survey of Optical Instruments* (Wiley-VCH, Weinheim, 2008).

16. E. Battistella, J. Schniete, K. Wesencraft, J. F. Quintana, G. McConnell, Light-sheet mesoscopy with the Mesolens provides fast sub-cellular resolution imaging throughout large tissue volumes. *iScience*. **25**, 104797 (2022).

17. R. Prevedel, Y. G. Yoon, M. Hoffmann, N. Pak, G. Wetzstein, S. Kato, T. Schrödel, R. Raskar, M. Zimmer, E. S. Boyden, A. Vaziri, Simultaneous whole-animal 3D imaging of neuronal activity using light-field microscopy. *Nat. Methods.* **11,** 727–730 (2014).

18. J. Demas, J. Manley, F. Tejera, K. Barber, H. Kim, F. M. Traub, B. Chen, A. Vaziri, High-speed, cortex-wide volumetric recording of neuroactivity at cellular resolution using light beads microscopy. *Nat. Methods.* **18,** 1103-1111 (2021).

19. E. Papagiakoumou, E. Ronzitti, V. Emiliani, Scanless two-photon excitation with temporal focusing. *Nat. Methods* **17**, 571–581 (2020).

20. F. F. Voigt, D. Kirschenbaum, E. Platonova, S. Pagès, R. A. A. Campbell, R. Kastli, M. Schaettin, L. Egolf, A. van der Bourg, P. Bethge, K. Haenraets, N. Frézel, T. Topilko, P. Perin, D. Hillier, S. Hildebrand, A. Schueth, A. Roebroeck, B. Roska, E. T. Stoeckli, R. Pizzala, N. Renier, H. U. Zeilhofer, T. Karayannis, U. Ziegler, L. Batti, A. Holtmaat, C. Lüscher, A. Aguzzi, F. Helmchen, The mesoSPIM initiative: open-source light-sheet microscopes for imaging cleared tissue. *Nat. Methods*. **16**, 1105–1108 (2019).

21. T. Nöbauer, Y. Zhang, H. Kim, A. Vaziri, Mesoscale volumetric light-field (MesoLF) imaging of neuroactivity across cortical areas at 18 Hz. *Nat. Methods*. **20**, 600–609 (2023).

22. A. Ichihara, T. Tanaami, K. Isozaki, Y. Sugiyama, Y. Kosugi, K. Mikuriya, M. Abe, I. Uemura, High-speed confocal fluorescence microscopy using a Nipkow scanner with microlenses for 3D-imaging of single fluorescent molecule in real time. *Bioimaging* **4**, 52–62 (1996).

23. M. Ishihara, A confocal surface measurement system having improved measurement accuracy for rough surfaces and measurement speed. *J. Robot. Mechatronics* **15**, 331–340 (2003).

24. M. Petráň, M. Hadravský, A. Boyde, The tandem scanning reflected light microscope. *Scanning* **7**, 97–108 (1985).

25. G. Q. Xiao, T. R. Corle, G. S. Kino, Real-time confocal scanning optical microscope. *Appl. Phys. Lett.* **53**, 716–718 (1988).

26. A. R. Halpern, M. Y. Lee, M. D. Howard, M. A. Woodworth, P. R. Nicovich, J. C. Vaughan, Versatile, do-it-yourself, low-cost spinning disk confocal microscope. *Biomed. Opt. Express.* **13**, 1102 (2022).

27. Z. Ma, J. Wang, P. Loskill, N. Huebsch, S. Koo, F. L. Svedlund, N. C. Marks, E. W. Hua, C. P. Grigoropoulos, B. R. Conklin, K. E. Healy, Self-organizing human cardiac microchambers mediated by geometric confinement. *Nat. Commun*. **61**. 6, 1–10 (2015).

28. P. Hofbauer, S. M. Jahnel, N. Papai, M. Giesshammer, A. Deyett, C. Schmidt, M. Penc, K. Tavernini, N. Grdseloff, C. Meledeth, L. C. Ginistrelli, C. Ctortecka, Š. Šalic, M.

797 Novatchkova, S. Mendjan, Cardioids reveal self-organizing principles of human
798 cardiogenesis. *Cell*. **184**, 3299-3317.e22 (2021).

799 29. Y. R. Lewis-Israeli, A. H. Wasserman, M. A. Gabalski, B. D. Volmert, Y. Ming, K. A.
800 Ball, W. Yang, J. Zou, G. Ni, N. Pajares, X. Chatzistavrou, W. Li, C. Zhou, A. Aguirre,
801 Self-assembling human heart organoids for the modeling of cardiac development and
802 congenital heart disease. *Nat. Commun*. **121**. 12, 1–16 (2021).

803 30. E. A. Susaki, K. Tainaka, D. Perrin, F. Kishino, T. Tawara, T. M. Watanabe, C.
804 Yokoyama, H. Onoe, M. Eguchi, S. Yamaguchi, T. Abe, H. Kiyonari, Y. Shimizu, A.
805 Miyawaki, H. Yokota, H. R. Ueda, Whole-brain imaging with single-cell resolution using
806 chemical cocktails and computational analysis. *Cell*. **157**, 726–739 (2014).

807 31. K. Tainaka, T. C. Murakami, E. A. Susaki, C. Shimizu, R. Saito, K. Takahashi, A.
808 Hayashi-Takagi, H. Sekiya, Y. Arima, S. Nojima, M. Ikemura, T. Ushiku, Y. Shimizu,
809 M. Murakami, K. F. Tanaka, M. Iino, H. Kasai, T. Sasaoka, K. Kobayashi, K. Miyazono,
810 E. Morii, T. Isa, M. Fukayama, A. Kakita, H. R. Ueda, Chemical Landscape for Tissue
811 Clearing Based on Hydrophilic Reagents. *Cell Rep*. **24**, 2196-2210.e9 (2018).

812 32. T. Hainmueller, M. Bartos, Dentate gyrus circuits for encoding, retrieval and
813 discrimination of episodic memories. *Nat. Rev*. *Neurosci*. **21**, 153–168 (2020).

814 33. M. Agetsuma, H. Aizawa, T. Aoki, R. Nakayama, M. Takahoko, M. Goto, T. Sassa, R.
815 Amo, T. Shiraki, K. Kawakami, T. Hosoya, S. I. Higashijima, H. Okamoto, The habenula
816 is crucial for experience-dependent modification of fear responses in zebrafish. *Nat.*
817 *Neurosci*. **13**, 1354–1356 (2010).

818 34. N. Dani, R. H. Herbst, C. McCabe, G. S. Green, K. Kaiser, J. P. Head, J. Cui, F. B.
819 Shipley, A. Jang, D. Dionne, L. Nguyen, C. Rodman, S. J. Riesenfeld, J. Prochazka, M.
820 Prochazkova, R. Sedlacek, F. Zhang, V. Bryja, O. Rozenblatt-Rosen, N. Habib, A.
821 Regev, M. K. Lehtinen, A cellular and spatial map of the choroid plexus across brain
822 ventricles and ages. *Cell*. **184**, 3056-3074.e21 (2021).

823 35. K. Sugawara, Ç. Çevrim, M. Averof, Tracking cell lineages in 3D by incremental deep
824 learning. *Elife*. **11**, 1–19 (2022).

825 36. S. Herculano-Houzel, R. Lent, Isotropic fractionator: A simple, rapid method for the
826 quantification of total cell and neuron numbers in the brain. *J. Neurosci.* **25**, 2518–2521
827 (2005).

828 37. Y. Sato, G. Poynter, D. Huss, M. B. Filla, A. Czirok, B. J. Rongish, C. D. Little, S. E.
829 Fraser, R. Lansford, Dynamic analysis of vascular morphogenesis using transgenic quail
830 embryos. *PLoS One*. **5**, e12674 (2010).

831 38. Y. Sato, Dorsal aorta formation: Separate origins, lateral-to-medial migration, and
832 remodeling. *Develop. Growth Differ.* **55**, 113–129 (2013).

833 39. E. Meijering, O. Dzyubachyk, I. Smal, Methods for cell and particle tracking. *Elsevier*
834 *Inc*. **504**, 183–200 (2012).

835 40. J. B. Beltman, A. F. M. Marée, R. J. De Boer, Analysing immune cell migration. *Nat.*
836 *Rev. Immunol*. **9**, 789–798 (2009).

837 41. J. R. Bumstead, J. J. Park, I. A. Rosen, A. W. Kraft, P. W. Wright, M. D. Reisman, D. C.
838 Côté, J. P. Culver, J. R. Bumstead, J. J. Park, I. A. Rosen, A. W. Kraft, P. W. Wright, D.
839 Reisman, D. C. Côté, J. P. Culver, M. D. Reisman, D. C. Côté, J. P. Culver, Designing a
840 large field-of-view two- photon microscope using optical invariant analysis microscope
841 using optical invariant analysis. *Neurophotonics*. **5**, 025001 (2018).

842 42. A. W. Lohmann, R. G. Dorsch, D. Mendlovic, C. Ferreira, Z. Zalevsky, Space–
843 bandwidth product of optical signals and systems. *J. Opt. Soc. Am. A*. **13**, 470 (1996).

844 43. K. Seiriki, A. Kasai, T. Nakazawa, M. Niu, Y. Naka, M. Tanuma, H. Igarashi, K.
845 Yamaura, A. Hayata-Takano, Y. Ago, H. Hashimoto, Whole-brain block-face serial
846 microscopy tomography at subcellular resolution using FAST. *Nat. Protoc.* **14**, 1509–
847 1529 (2019).

848 44. S. Takanezawa, T. Saitou, T. Imamura, Wide field light-sheet microscopy with lens-
849 axicon controlled two-photon Bessel beam illumination. *Nat. Commun.* **12**, 2979 (2021).

850 45. L. Hof, T. Moreth, M. Koch, T. Liebisch, M. Kurtz, J. Tarnick, S. M. Lissek, M. M. A.
851 Verstegen, L. J. W. van der Laan, M. Huch, F. Matthäus, E. H. K. Stelzer, F. Pampaloni,

852 Long-term live imaging and multiscale analysis identify heterogeneity and core principles
853 of epithelial organoid morphogenesis. *BMC Biol*. **19**, 1–22 (2021).

854 46. H. -C. Lee and G. Yang, Computational removal of background fluorescence for
855 biological fluorescence microscopy. *IEEE 11th International Symposium on Biomedical*
856 *Imaging (ISBI),* 205–208, doi: 10.1109/ISBI.2014.6867845 (2014).

857 47. K. Walter, F. Ziesche, Apparatus and Method, Particularly for microscopes and
858 endoscopes, using baseline estimation and half-quadratic minimization for the deblurring
859 of images, WO 2019/185174 A1. European Patent Office (2019).

860 48. P. Getreuer, A Survey of Gaussian Convolution Algorithms. *Image Process. Line*. **3**,
861 286–310 (2013).

862 49. A. Hyvaerinen, J. Karhunen, E. Oja, Independent Component Analysis (Adaptive and
863 Cognitive Dynamic Systems: Signal Processing, Learning, Communications and Control)
864 (Wiley-Interscience, New York, 2021).

865 50. M. Nakagawa, Y. Taniguchi, S. Senda, N. Takizawa, T. Ichisaka, K. Asano, A.
866 Morizane, D. Doi, J. Takahashi, M. Nishizawa, Y. Yoshida, T. Toyoda, K. Osafune, K.
867 Sekiguchi, S. Yamanaka, A novel efficient feeder-Free culture system for the derivation
868 of human induced pluripotent stem cells. *Sci. Rep*. **4**, 1–7 (2014).

869 51. P. W. Burridge, E. Matsa, P. Shukla, Z. C. Lin, J. M. Churko, A. D. Ebert, F. Lan, S.
870 Diecke, B. Huber, N. M. Mordwinkin, J. R. Plews, O. J. Abilez, B. Cui, J. D. Gold, J. C.
871 Wu, Chemically defined generation of human cardiomyocytes. *Nat. Methods*. **11**, 855–
872 860 (2014).

873 52. E. A. Susaki, C. Shimizu, A. Kuno, K. Tainaka, X. Li, K. Nishi, K. Morishima, H. Ono,
874 K. L. Ode, Y. Saeki, K. Miyamichi, K. Isa, C. Yokoyama, H. Kitaura, M. Ikemura, T.
875 Ushiku, Y. Shimizu, T. Saito, T. C. Saido, M. Fukayama, H. Onoe, K. Touhara, T. Isa, A.
876 Kakita, M. Shibayama, H. R. Ueda, Versatile whole-organ/body staining and imaging
877 based on electrolyte-gel properties of biological tissues. *Nat. Commun.* **11**, 1982 (2020).

878 53. V. Hamburger, H. L. Hamilton, A series of normal stages in the development of the chick
879 embryo. *J. Morphol.* **88**, 49–92 (1951).

880 54. Y. Sato, R. Lansford, Transgenesis and imaging in birds, and available transgenic
881 reporter lines. *Develop. Growth Differ.* **55**, 406–421 (2013).

882 55. J. M. Mateos-Pérez, R. Redondo, R. Nava, J. C. Valdiviezo, G. Cristóbal, B. Escalante-
883 Ramírez, M. J. Ruiz-Serrano, J. Pascau, M. Desco, Comparative evaluation of autofocus
884 algorithms for a real-time system for automatic detection of Mycobacterium tuberculosis.
885 *Cytom. Part A*. **81 A**, 213–221 (2012).

886 56. https://github.com/elephant-track

887 57. https://github.com/mastodon-sc/mastodon

888 58. J. Schindelin, I. Arganda-Carreras, E. Frise, V. Kaynig, M. Longair, T. Pietzsch, S.
889 Preibisch, C. Rueden, S. Saalfeld, B. Schmid, J. Y. Tinevez, D. J. White, V. Hartenstein,
890 K. Eliceiri, P. Tomancak, A. Cardona, Fiji: An open-source platform for biological-image
891 analysis. *Nat. Methods.* **9**, 676–682 (2012).

892 59. T. Pietzsch, S. Saalfeld, S. Preibisch, P. Tomancak, BigDataViewer: visualization and
893 processing for large image data sets. *Nat. Methods.* **12**, 481–483 (2015).

894 60. https://github.com/bigdataviewer/bigdataviewer-server

895 61. E. Moen, D. Bannon, T. Kudo, W. Graf, M. Covert, D. Van Valen, Deep learning for
896 cellular image analysis. *Nat. Methods.* **16**, 1233–1246 (2019).

897 62. C. Wen, T. Miura, V. Voleti, K. Yamaguchi, M. Tsutsumi, K. Yamamoto, K. Otomo, Y.
898 Fujie, T. Teramoto, T. Ishihara, K. Aoki, T. Nemoto, E. M. C. Hillman, K. D. Kimura,
899 3Deecelltracker, a Deep Learning-Based Pipeline for Segmenting and Tracking Cells in
900 3D Time Lapse Images. *Elife*. **10**, 1–37 (2021).

901

ACKNOWLEDGMENTS

We would like to thank Prof. K. Fujita of Department of Applied Physics, Osaka University, Japan for his valuable comments on optics design. We are also grateful to Prof. S. Miyagawa, and Prof. Y. Sawa of Graduate School of Medicine, Osaka University, for their support on handling human iPS cells and valuable discussion.

Funding:

Grant-in-Aid for Scientific Research on Innovative Areas “Singularity Biology (No. 8007)” 21H00431 (YS), 18H05416 (HH), 18H05412 (SO), and 18H05410, 18H05408 (TN)

Grant-in-Aid for Transformative Research Areas (A) “Seeing through Scattering Media (No. 20A207)” 21H05590 and 23H041350 (TI)

the Research Program of "Five-star Alliance" in "NJRC Mater. & Dev." (TN)

Precursory Research for Embryonic Science and Technology (PRESTO) JPMJPR18G2 (TI)

JSPS KAKENHI JP23H00395 and JP24K22022 (HH)

AMED Brain/MINDS JP21dm0207117 (HH) and BINDS JP23ama121054 and JP23ama121052 (HH)

The Uehara Memorial Foundation (TN)

Takeda Science Foundation (TN, HH)

Core Research for Evolutionary Science and Technology (CREST) JPMJCR15N3 (TN), JPMJCR1926 (KS, SO)

RIKEN Cluster for Science, Technology and Innovation Hub (SO)

JST NBDC Grant Number JPMJND2201 (SO)

Author contributions:

Conceptualization: TI, TN

Optics design: TI, HH, TN, YT, SE

Lens design and fabrication: YT

Optical system construction: TI, YT, SE

Development of imaging system software: TI

Sample preparation: TK, YS, KS, HH

Data acquisition: TK, YS, TI

Data analysis and visualization: KI, TI, TK, KS

Setup of deep-learning platform: KS, HI, SO

Construction of data share server: HI, SO

Writing—original draft: TI

Writing—review & editing: TI, TN

Competing interests:

T.I, H.H and T.N have patent applications (2021-104163(JP), 2023-077341). K.S. is employed part-time by LPIXEL Inc. All other authors declare no additional conflict of interests.

Data and materials availability:

All data needed to evaluate the conclusions in the paper are present in the paper and/or Supplementary Materials.

948 **FIGURES**

949

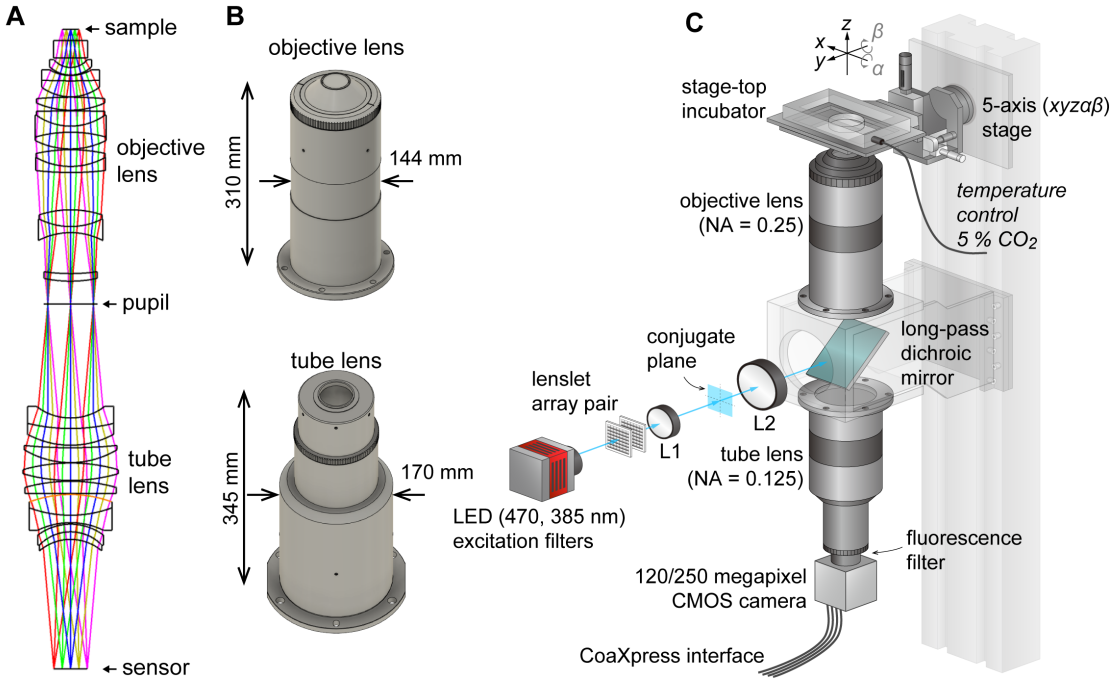

950

951 **Fig. 1. AMATERAS-2, a centimeter-FOV cell-imaging system** (A) Schematics of the
952 design of the objective and tube lenses for AMATERAS-2. (B) Appearance of the objective
953 and tube lenses with the width and length. (C) Diagram of the wide-field fluorescence
954 imaging system, AMATERAS-2w, using the two lenses in (A-B). See Materials and Methods
955 for detail.

956

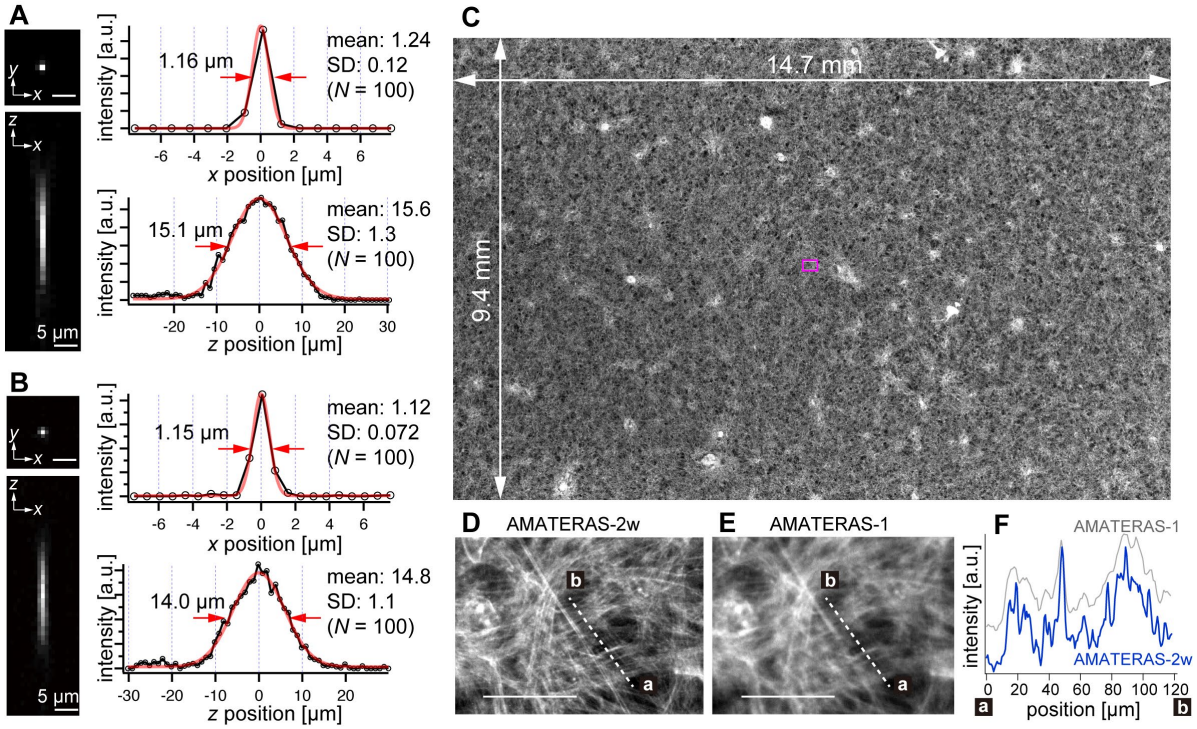

Fig. 2. Optical performance of AMATERAS-2w (A),(B) Experimentally obtained PSF of green fluorescent beads with a 0.2-µm diameter in the *xy* and *xz* planes, captured using CMOS cameras with (A) 120 megapixels (pixel size = 2.2 µm) and (B) 250 megapixels (pixel size = 1.5 µm). The representative line profiles in the *x* and *z* directions on the beads are shown (black lines with circular markers) along with Gaussian fit curves (red lines) and FWHMs, and the mean and standard deviation (SD) calculated for 100 beads are described beside each profile. (C) Fluorescence image of a cardiomyocyte sheet in the entire FOV. (D) Digitally magnified view of the area indicated by a magenta square at the center of (C); scale bar, 100 µm. (E) Same area as (D) but observed by AMATERAS-1 for comparison. (F) Line profiles of the lines in (D) and (E) for comparison of spatial resolution.

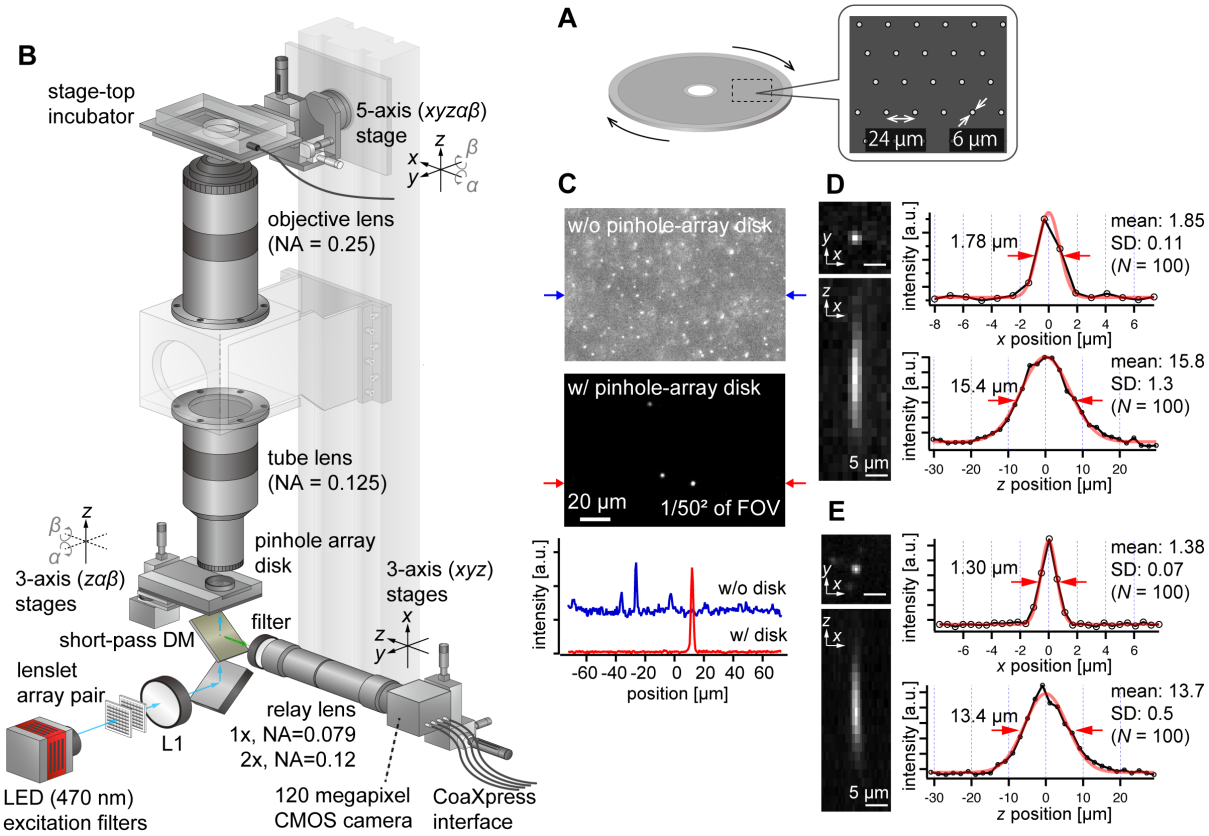

Fig. 3. AMATERAS-2c, a multipoint confocal imaging system for 3D volume imaging. (A) Design of our pinhole-array disk. (B) Schematic of the optical configuration using the pinhole-array disk. (C) Effect of background light rejection by the presence of the pinhole-array disk in a 292 × 202 µm^2 area at the FOV center corresponding to 1/50^2 of the entire FOV. (D),(E) Experimentally obtained PSF of green fluorescent beads with a diameter of 0.5 µm in the *xy* and *xz* planes, captured using relay lens with (D) 1× magnification (NA = 0.079) and (E) 2× magnification (NA = 0.12). The representative line profiles in the *x* and *z* directions on the beads are also shown (black lines with circular markers) along with Gaussian fit curves (red lines) and FWHMs, and the mean and standard deviation (SD) calculated for 100 beads are described beside each profile.

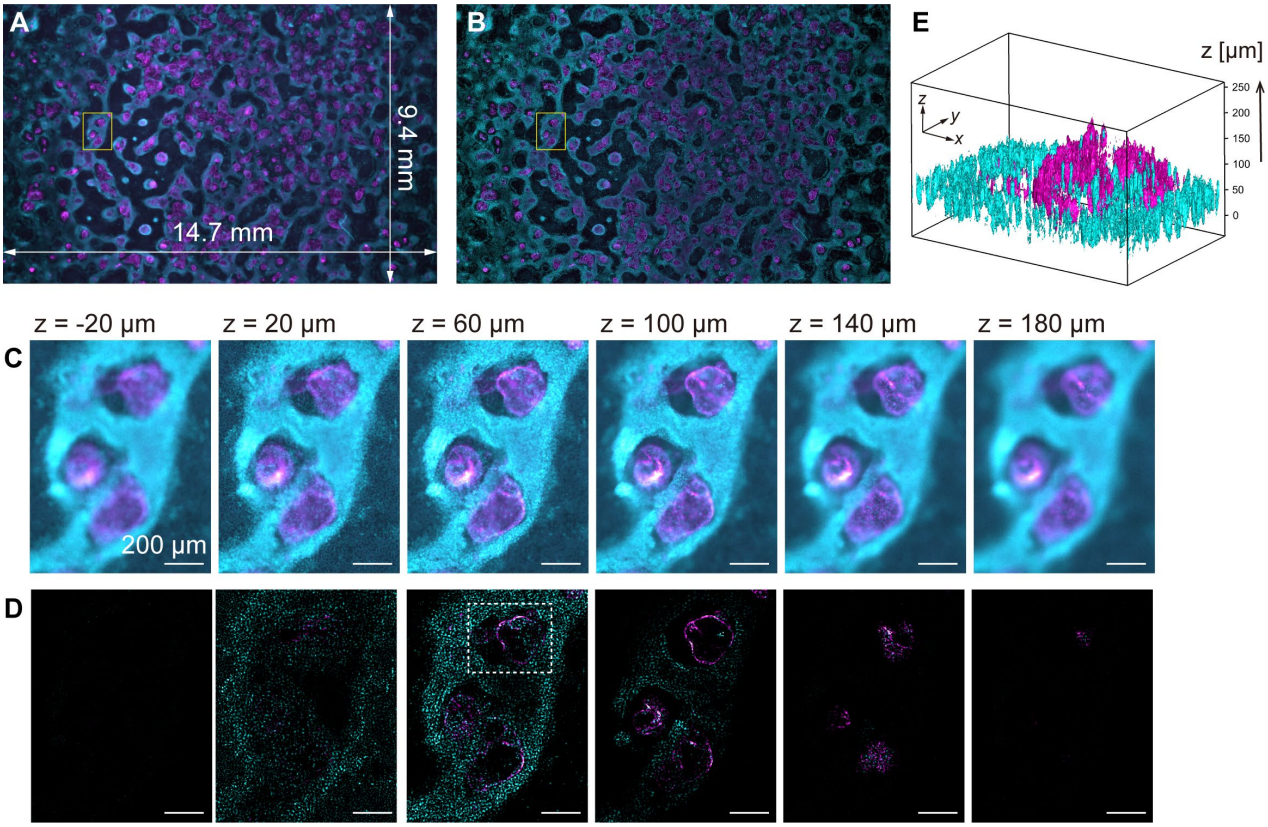

Fig. 4. Volumetric imaging with computational sectioning. (A),(B) Two-color images of the cavity chamber structure of a myocardial organoid (A) before and (B) after computational sectioning. Both (A) and (B) are MIP images of the *z*-stack data, captured using the 250-megapixel CMOS camera; here, magenta and cyan represent the distribution of immunostained cardiac troponin T and Hoechst-labeled nuclei, respectively. (C),(D) Six z-layers with a difference of 40 μm in the yellow square region indicated in (A),(B); scale bars, 200 μm. (E) Three-dimensional isosurface representation in the dashed square region indicated in (D).

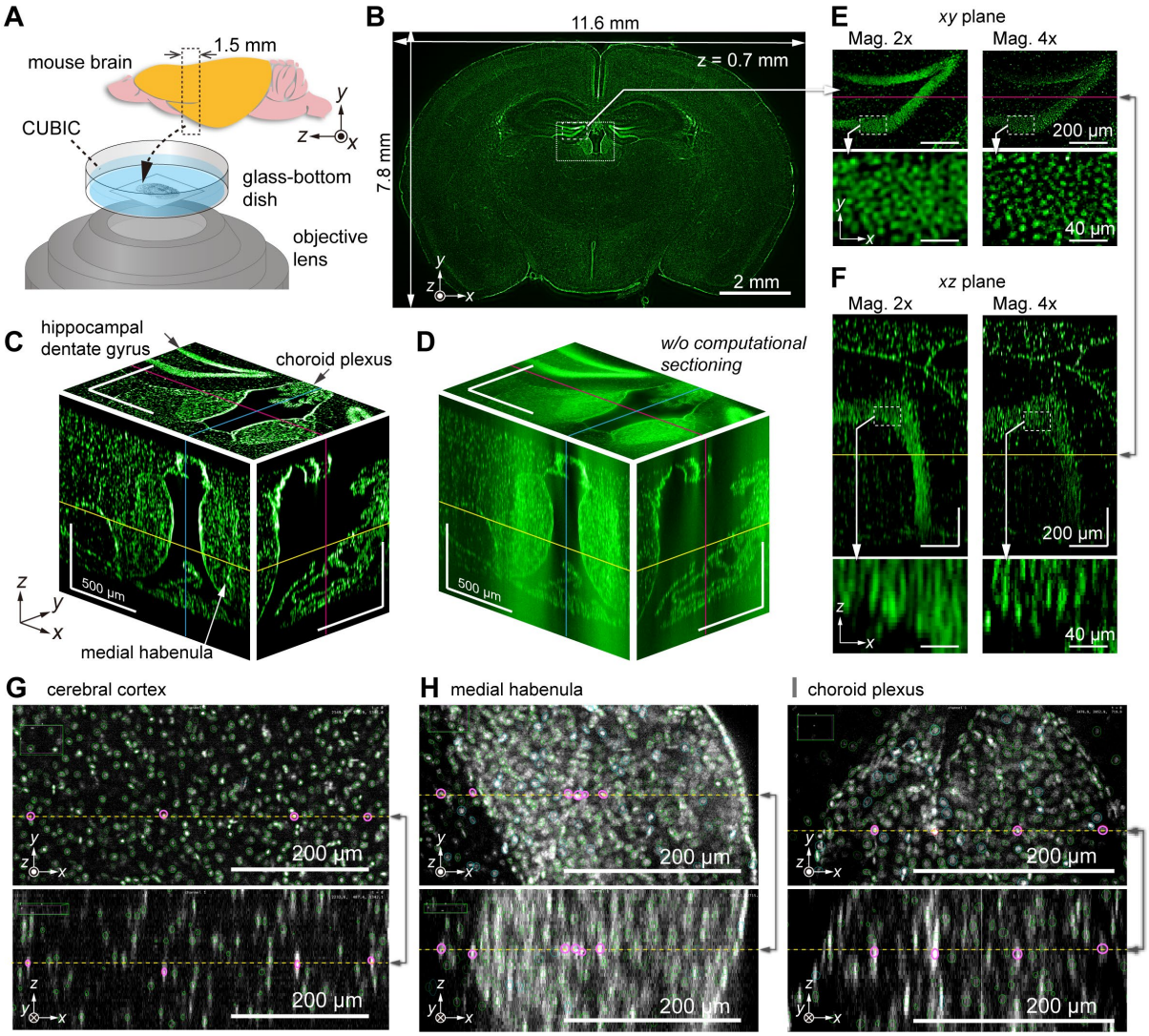

Fig. 5. Volumetric imaging of a mouse brain section. (A) Schematic of a mouse brain showing the placement of the brain sample in the inverted configuration. (B) Schematic of a single *z*-layer in the coronal plane with size of the effective area covering the entire brain section. (C) Fluorescence images of three orthogonal cross sections of the dotted square indicated in (B); here, the yellow, cyan, and magenta lines represent the *z*-, *x*-, and *y*-positions of the cross sections, respectively. (D) Cross-sectional images of raw data in the same region as (C), where the computational sectioning is not applied. (E),(F) Magnified images of the hippocampal region (dashed square in (B)) in the (E) *xy*-plane and (F) *xz*-plane. For comparison, images obtained with 2× (left) and 4× (right) magnification systems are shown together. Note that the 3D regions observed at different magnifications do not perfectly match owing to the difficulty in optical alignment. (G-I) Cell detection by ELEPHANT in three brain regions, the cerebral cortex (G), medial habenula (H), and choroid plexus (I), where

1004 pairs of intersecting *xy*- and *xz*-planes are arranged vertically. The detected cells within each
1005 plane are marked with green and cyan ovals, and the straight line shared by the two planes is
1006 represented by a yellow dashed line, with certain cells along this line highlighted by magenta
1007 ovals. The *xy*-planes overlay the oval markers within a range of ± 25 μm above and below the
1008 focal plane, while the *xz*-plane shows only oval markers on the plane.
1009

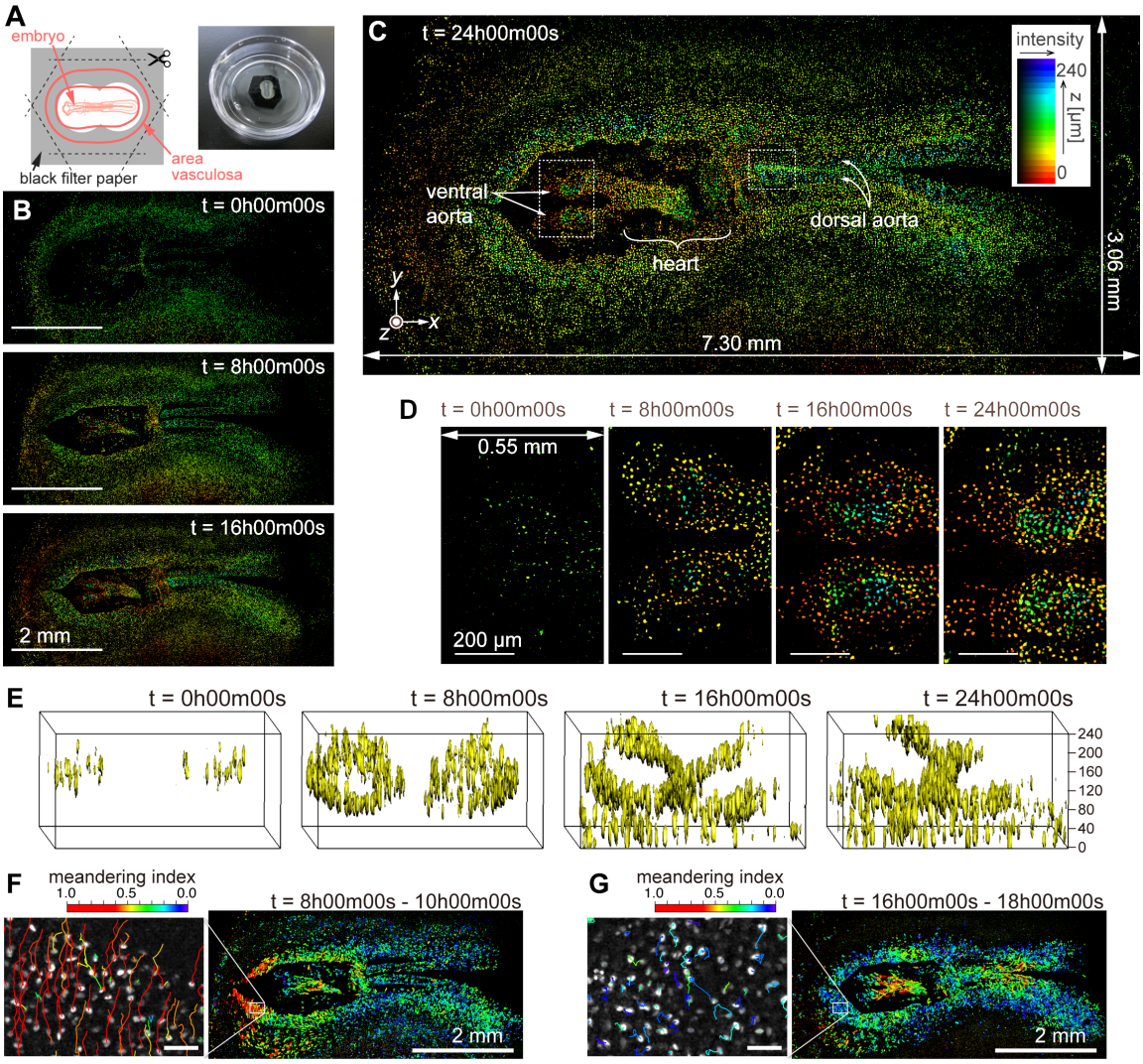

Fig. 6. Dynamics of vascular endothelial cells in quail embryo captured by time-lapse observation. (A) Schematic showing how the specimen is mounted (left) and a photograph of a specimen placed in a glass-bottom dish. (B) Representative images obtained at $t = 0$ h, 8 h, and 16 h; scale bars, 2 mm. (C) Enlarged view of the image corresponding at $t = 24$ h; the pseudo-colors represent the z-position of the cells and fluorescence intensity by their hue and brightness, respectively. (D) Magnified views of the anterior side of ventral aortae (left dashed square in (C)) at the four time-points with intervals of 8 h; scale bars, 200 μm. (E) Three-dimensional isosurface representation of the dorsal aorta region (right dashed square in (C)) viewed from the left side. (F),(G) Cell position trajectories and spatial mapping of features related to the cell dynamics in the two time-regions of (F) $t = 8$–10 h and (G) $t = 16$–18 h. Left panels show enlarged views in the white square regions (292×202 μm^2) indicated in the right panels. In both the panels, the rainbow-colored trajectories of the cell movement

1023 are overlaid on the grayscale MIP images at the first frame in the time regions (F: t = 8 h, G: t
1024 = 16 h). The scale bars are 50 μm. The rainbow color table represents the meandering index
1025 of the cell movement in the two time-regions.
1026